Building and Environment 178 (2020) 106930

Contents lists available at ScienceDirect

Building and Environment

journal homepage: http://www.elsevier.com/locate/buildenv

3D real-time volumetric particle tracking velocimetry – A promising tool for studies of airflow around high-rise buildings

Yu Zhao [a], Xiaojun Ma [b], Chengbin Zhang [a], Haoyu Wang [b], Yuanhui Zhang [a,*]

[a] Department of Agricultural and Biological Engineering, University of Illinois at Urbana-Champaign, Urbana, United States
[b] College of Biochemical Engineering, Beijing Union University, Beijing, China

ARTICLE INFO

Keywords:
Volumetric particle tracking velocimetry (VPTV)
Building wind environment
Flow pattern measurement
Real-time

ABSTRACT

Airflow patterns around high-rise buildings affect building wind environment (BWE) including infiltration/exfiltration, heating/cooling loads and internal environment. Scaled high-rise building models are usually placed in a wind tunnel to study BWE. However, measuring 3D flow patterns around scaled high-rise buildings in real-time is a challenge. In this study, a 3D real-time Volumetric Particle Tracking Velocimetry (VPTV) system was used to measure the airflows around three different scaled-building setups: single building, double building parallel to the wind, and double building perpendicular to the wind. Trajectories in Lagrangian coordinates system were tracked and then interpolated to generate 3D Eulerian description of the flow field. In this study, the relative errors of velocities measured by VPTV were smaller than 2% for magnitudes range from 0.025 m/s to 2.2 m/s. The local velocity magnitudes measured by hot-wire anemometer and CFD at selected positions were compared with VPTV measurement with relative error 26.2% and 16.3% respectively. Finally, measured streamlines and reattachment lengths were compared with CFD simulation at selected plane. Results show that the VPTV system is capable of capturing detailed and accurate data of airflow around scaled high-rise building models.

1. Introduction

With the global economic development and urbanization, many more high-rise buildings have been built in city centers, not only as a symbol of modern aesthetics and economic development but also for land efficiency [1]. At the same time, negative impacts on human and environment begin to appear. High-rise buildings could amplify wind speed under certain circumstances, which would cause safety hazards or reduce comfort for the pedestrians. In some other cases, they could cause local vortex and airflow dead-zone, which would accumulate pollutants and be harmful to health [2]. In addition, building energy consumption can be increased by poorly designed wind environment around high-rise buildings, because the infiltration/exfiltration due to wind pressure would increase heating and cooling loads [3,4]. Therefore, the wind environment around buildings, especially high-rise buildings, should be considered at the stage of planning. Many countries have developed their own building environmental assessments to guide the building environment design such as LEED [5] and BREEAM [6]. At prediction stage, the BWE design could be optimized to avoid potential defects such as air eddy, dead space and channel effect. Thus, it is important to have a full understanding of high-rise building wind environment before the construction.

Currently there are two methods of BWE prediction: scaled-model experiment and numerical simulation. The scaled-model experiment is usually conducted in a wind tunnel to study the influences of wind environment on high-rise buildings, residential neighborhoods and urban districts [7–9]. The experimental method obtains data directly from real measurement but is limited by factors including point by point measurement and interference to the flow field. Computational fluid dynamics (CFD), as the most popular numerical simulation method, is widely used in building wind environment prediction. It is fast, inexpensive, friendly for visualization and can obtain comprehensive data and information than the traditional experimental methods [10–14]. However, given the complexity of the boundary conditions and fluctuation of the airflow field, it is difficult to have a reliable and accurate simulation, unless the model is carefully calibrated using measurement data.

Besides the point by point measurement methods, there are several imaging techniques for measuring velocity field such as Particle Image Velocimetry (PIV), Particle Streak Velocimetry (PSV) and Particle

* Corresponding author.
E-mail address: yzhang1@illinois.edu (Y. Zhang).

https://doi.org/10.1016/j.buildenv.2020.106930
Received 13 March 2020; Received in revised form 17 April 2020; Accepted 28 April 2020
Available online 5 May 2020

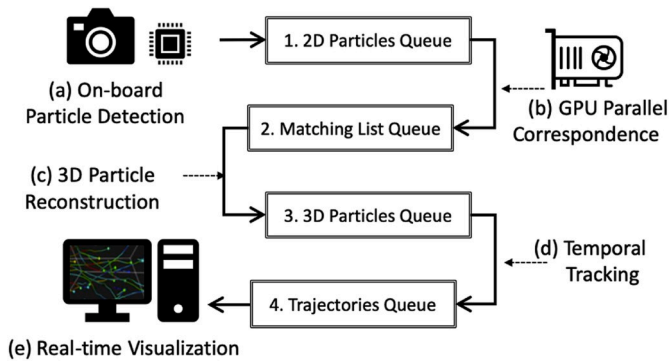

Fig. 1. VPTV data pipeline and the tasks applied on datasets: (a) On-board Particle Detection for fast particle centroids extraction; (b) Parallel image correspondence in GPU; (c) Reconstruction of 3D Particle coordinates from the matched images; (d) Temporal tracking of adjacent frames to extend existing trajectories or generate new trajectories; (e) Real-time visualization of tracked trajectories and flow field.

Tracking Velocimetry (PTV). All three methods share many similarities but are different in terms of particle density and computation method. When the particle density is too high to track single particle, PIV is usually used to statistically calculate the velocity of a fixed Eulerian integration window [15] by cross-correlation of particles images [16]. Typically, 2-D velocity vectors are acquired through PIV as only one camera is used to capture tracing particles within a plane illuminated by thin laser sheet. Stereoscopic PIV [17] was developed to capture 3-D velocity vector at several planes illuminated by thin light sheet, however it still cannot cover whole 3-D measurement volume. Tomographic PIV [18] was developed to acquire 3-D intensity of measurement volume but the computation load is too intense to measure in real-time.

When the particle density is relatively low, single particle trajectories can be tracked by PSV or PTV. PSV uses long exposure time to capture path lines of particles on 2-D camera image [19]. In PSV, velocity is calculated according to time interval and displacement from start to end points of 2-D trajectory. However, error will be introduced because path lines of particles are usually twisted for turbulent flow and the calculation of velocity is not accurate. A color sequence PSV was developed [20] to gain more information of particle path lines by using a color

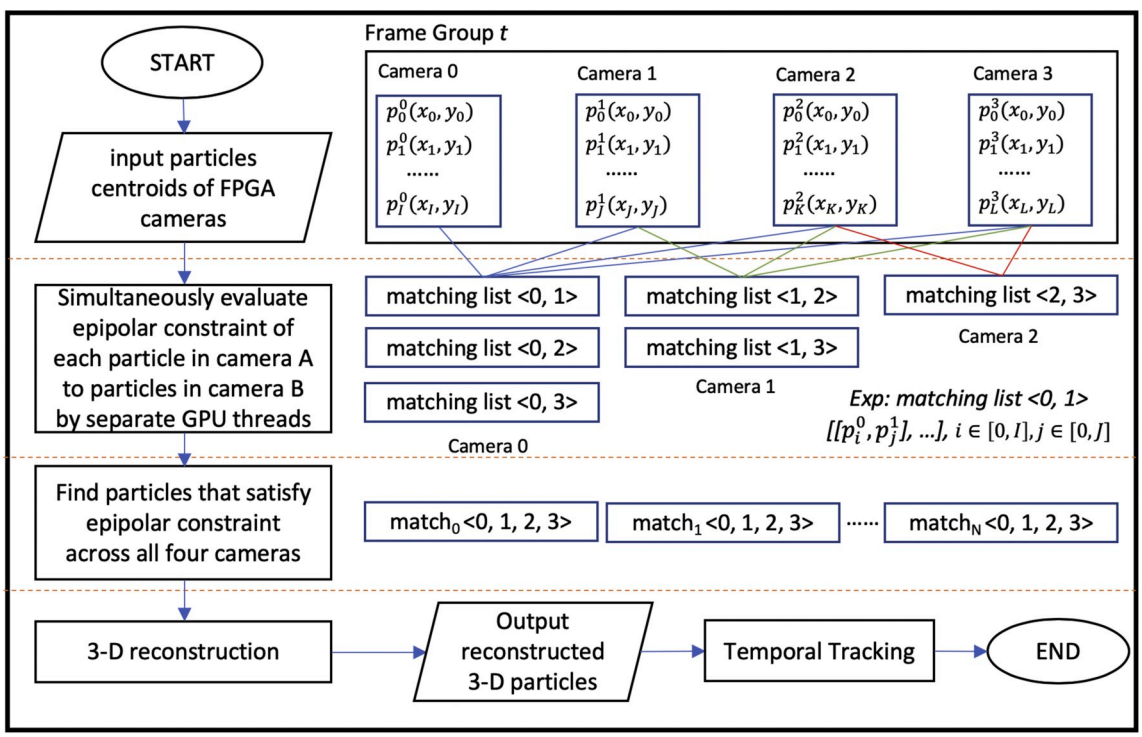

Fig. 2. A flow chart of processes applied in one frame group at timestep t.

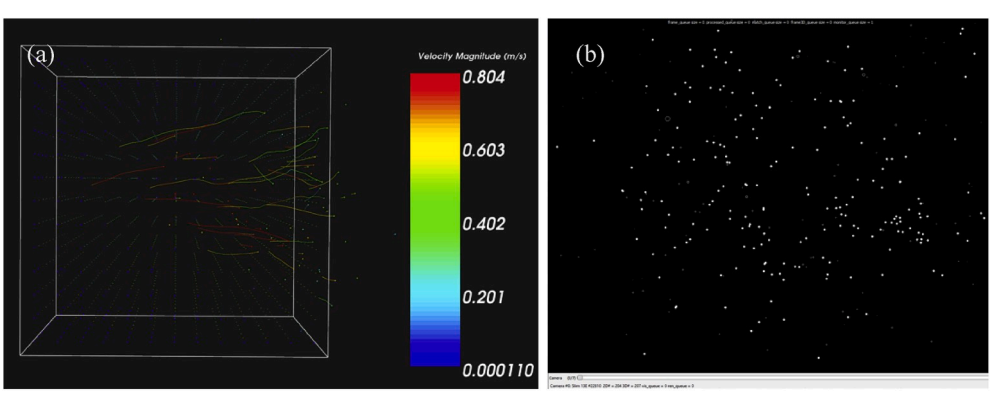

Fig. 3. Screenshots of the VPTV measurement: (a) 3D trajectories tracked at one instant time; (b) Detected particles by one camera.

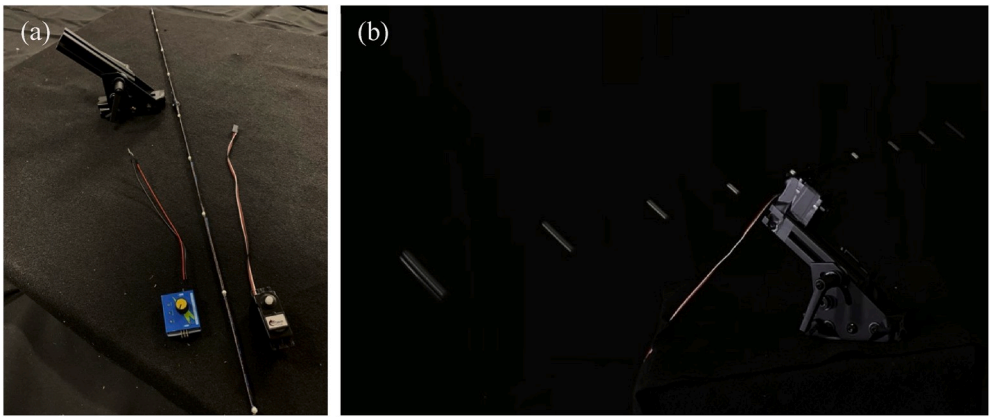

Fig. 4. The diagram of calibration setup: (a) Servo Motor and reflective beads; (b) Reflective beads are rotating with a given angular velocity.

sequence LED to mark particle spots on path line. The velocity can be calculated more accurately because of higher temporal resolution. However, synchronizing the LED light and cameras becomes an overwhelming challenge.

Particle Tracking Velocimetry (PTV) is a method measuring flow field by tracking tracing particles based on Lagrangian Particle Tracking (LPT) specification. PTV is similar to PSV but it utilizes much shorter exposure time than PSV. PTV is typically used in low particle density case, however it has recently been used in higher particle density case, where more than 100,000 particles per image (~0.1 particle per pixel) were tracked by a time-resolved iterative tracking algorithm [21].

PTV is able to track 3-D particle trajectories instead of 2-D trajectories captured in PSV. The tracked 3-D particle trajectories are then interpolated onto the Eulerian coordinate system to produce a flow field profile. Multiple cameras with high resolution are recommended to ensure 3-D reconstruction of particles. However, more cameras and higher frame rates will increase the cost of memory and computation, as enormous images need to be stored first and analyzed afterwards. To solve this problem, cameras equipped with field-programmable gate array (FPGA) [22] and parallel tracking algorithm [23] have been developed and applied in PTV to allow fast and high-resolution image capturing.

To overcome the aforementioned shortcomings of imaging measurement techniques such as lacking of 3-D information, high memory requirement and intense computation load, a real-time, 3-dimensional Volumetric Particle Tracking Velocimetry (VPTV) system has been developed in our lab [24], which takes advantage of FPGA cameras and parallel computing to achieve real-time measurement and visualization. In particular, FPGA cameras calculate the tracing particles' centroids on-board without involving computer image processing and thus the data flow size can be reduced by 1000 times compared with the PTV system using traditional cameras [22]. To further accelerate particle tracking process, parallel computing utilizing multiple CPUs and GPUs is implemented in this system to reduce the data accumulation from particle detection and multi-camera correspondence. This system is capable of tracking a flow field with 200 particles/image at 120/s frame rate in real-time with 8 cameras using a personal computer equipped with Intel i5-8400 CPU and NVIDIA RTX 2060 GPU.

After decades of development, PTV methods have been used to measure different flow fields ranging from nanometer scale [25] to meter scale [26]. Due to the low data flow rate, additional FPGA cameras can be added to this system to increase the measurement volume, which would broaden the applications of VPTV from small scale ($<1\ m^3$) to much larger scale (full room size). Theoretically, up to 254 FPGA cameras can be synchronized and programmed into our VPTV system to increase measurement volume. The real-time measurement allows realistic visualization of flow field with much more information than traditional fluid visualization methods such as single point anemometry and tracer method. This VPTV system has been used in a nozzle airflow study, and the measurements results match well with theoretical calculation and other measurements [27].

Although other similar methods such as PSV [20] and PIV [28] have been developed and used in indoor and outdoor BWE studies, to the best of our knowledge, real-time 3-D PTV measurement of scaled building model has not been reported in BWE study yet. Due to the facts that measurement volume in BWE study is generally large and simple illumination source is preferred, VPTV would be a promising tool for BWE study because its scalability of cameras enlarges the measurement volume and the low dependence to specific light source simplifies the illumination setup.

In this study, airflows around three building setups were measured by real-time 3-D VPTV: single building, double building parallel to the wind and double building perpendicular to the wind. This VPTV system was calibrated by measuring known trajectory velocities before measurement. The detailed experiments are as follows: Firstly, the trajectories tracked by VPTV were interpolated to Eulerian coordinate system to generate local velocity distribution. Secondly, local velocities at selected points in measurement volume were compared with results measured by hot-wire anemometer and results simulated by CFD. Finally, streamlines and reattachment lengths around building models measured by VPTV were compared with CFD simulation. The results show that VPTV system is a promising method for studies of airflow around various building model setups. The spatial scalability and real-time characteristic make this system flexible for BWE study, and the results measured by VPTV are informative and accurate compared to other methods.

2. Methods and experimental design

2.1. 3D real-time VPTV system

This VPTV system is designed to achieve real-time visualization of a flow field. The main characteristics of this VPTV system are shown in Fig. 1. A data pipeline is used to connect five main tasks of VPTV: (a) particle detection, (b) image correspondence, (c) 3D reconstruction, (d) temporal tracking and (e) visualization. Particle tracking data are pumped into this data pipeline by a First-in-First-out strategy, and each task is assigned separate CPU process. The whole data pipeline consists of four different queues: 1. 2D Particles Queue inputs particles' centroids extracted from different cameras and pop out for correspondence; 2. Matching List Queue inputs the four-camera matched particles indexes and pop out for 3D reconstruction; 3. 3D Particles Queue inputs reconstructed 3D particles coordinates and pop out for temporal tracking; 4. Trajectories Queue inputs currently tracked trajectories waiting for visualizer to perform real-time visualization.

In the measuring process, the two most time-consuming tasks are

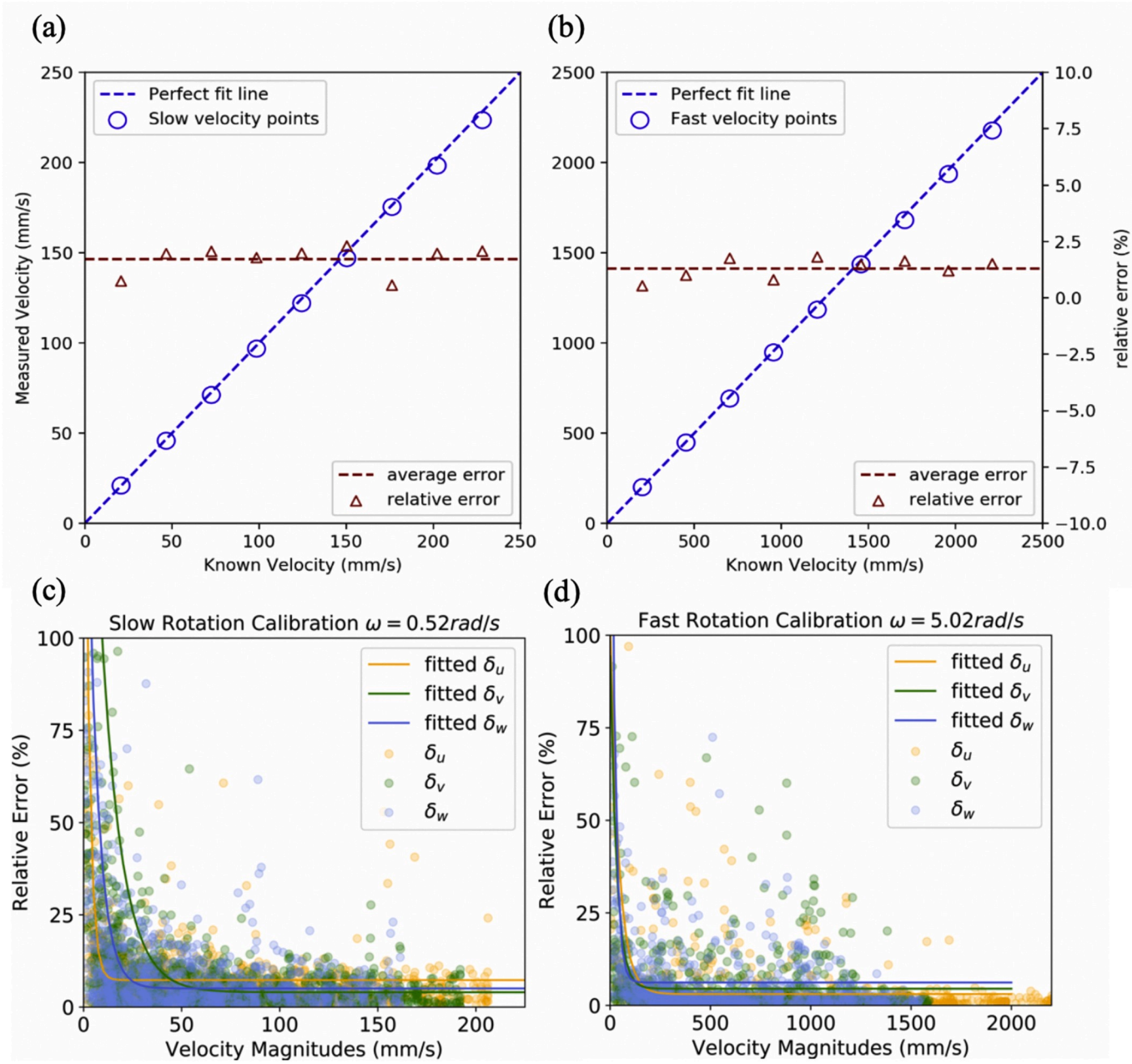

Fig. 5. Relative errors of different velocity ranges: (a) The average velocities for nine reflective beads measured by VPTV with known velocities range from 0.025 m/s to 0.225 m/s, and the mean relative error is 1.7%; (b) The velocities measured by VPTV with known velocities range from 0.2 m/s to 2.2 m/s, and the mean relative error is 1.3%; (c) Relative error of three velocity components magnitudes in slow velocity range; (d) Relative error of three velocity components magnitudes in fast velocity range.

particle detection and correspondence of particles among different cameras [24]. To achieve real-time visualization, data accumulation of above two tasks should be avoided. To cut down the particle detection time, cameras equipped with FPGA are used. FPGA camera allows on-board particle image segmentation and only the centroid pixel coordinates of each particle are sent to workstation instead of the raw particle grayscale image. In this VPTV system, eight 240 Hz maximum frame rate Optitrack Slim 13E cameras with 1280 × 1024 pixels were used.

The second task that causes data accumulation is camera correspondence. A four-camera correspondence criterion [29] was used in this system to enhance the accuracy. To cut down correspondence time, this algorithm was divided into two subtasks: 1. correspondence of particle in every two cameras; 2. Identify particle that is corresponded in every four cameras. For the first subtask, it is of highly parallelism as there is no time dependence. For example, the epipolar constraint of a particle in camera A can be simultaneously computed with particles in camera B, C, and D. In addition, epipolar constraint of each particle in camera A can be simultaneously computed with each particle in camera B, C or D. To accelerate this task, this VPTV system takes advantage of parallelism in the first subtask by using Graphics Processing Units (GPU), as it is suitable for calculating same operation on different data. In parallel implementation of the first subtask, each particle in camera A is assigned a GPU thread to iterate and correspond all other particles in camera B. This significantly improves the corresponding speed as all threads can proceed without time dependence. The GPU implementation is done with NVIDIA's Compute Unified Device Architecture (CUDA) programming paradigm, which is an extension of the C/C++

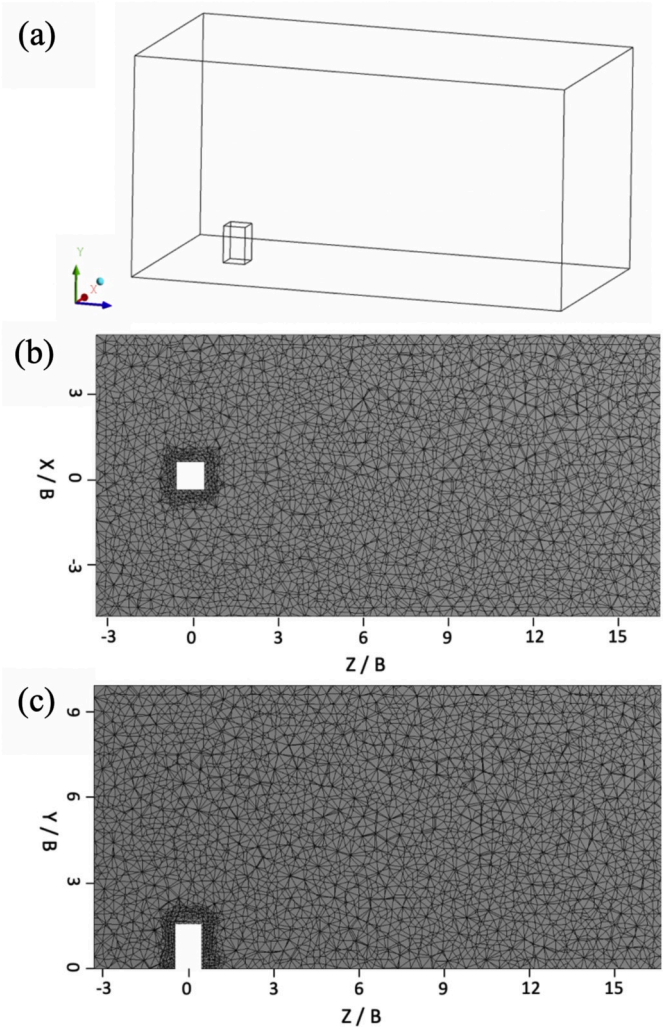

Fig. 6. (a) Computation domain of CFD simulation; (b) The mesh of cross-section Y = 0.5 H; (c) The mesh of cross-section X = 0.

language to allow efficient programming of GPU for general computation purposes. A flow chart of how one frame group at timestep t is processed by four cameras in VPTV system is shown in Fig. 2.

Two screenshots at one instant are shown in Fig. 3. There were approximately 250 particles in camera and 230 of which were reconstructed in the 3D space. There was no data accumulation in data pipeline and thus the flow field can be visualized in real-time. Tracked trajectories were smoothed by cubic spline method, and velocity was calculated by the derivative of smoothed trajectories. Lagrangian velocity was then interpolated onto Eulerian grid with width 40, height 20 and depth 40 cells respectively. Each Eulerian grid was a cubic cell with a side length of 50 mm. The measurement continued for 30–60 min. The Measurement Volume was 4 m^3 with width 2 m, height 2 m and depth 1 m. The frame rates of cameras were set to 60 frames/s.

2.2. Calibration of the VPTV measurement

Errors of VPTV can be caused by camera distortion, particle detection, correspondence, 3-D reconstruction and particle temporal tracking. To correct the projection error from distorted image, a 4× 11 circle grid was used to calibrate cameras according to Zhang's method [30]. Particle detection is another task that could introduce large uncertainties and errors [24]. To eliminate the error caused by particle detection, several on-board image processing modes are provided by FPGA cameras from high accuracy and high CPU usage to low accuracy but low CPU usage. To achieve a balance between particle centroid detection accuracy and computation load, "Object" mode was used in our system, which uses weight averaging for particle centroid calculation similar to that described by Biwole et al. [31]. For correspondence and 3-D reconstruction, additional cameras can increase the possibility of a particle being reconstructed in 3-D space [29], in particular, four cameras versus less. Less than four cameras reconstruction criterion was used in some research to ensure that a particle is reconstructed [21], however, this approach sacrificed reconstruction accuracy. In this study, eight cameras were used to increase the intersection volume between cameras. Each reconstructed particle was corresponded by four cameras and thus higher accuracy was achieved. For particle trajectory tracking, a 2-D minimum acceleration multi-frame regression algorithm robust to noise was developed in our group [32], and it was extended to 3-D and implemented in this VPTV system [24]. With multiple sources of errors, a calibration stage is necessary to determine the accuracy of this VPTV system.

To calibrate this VPTV system, a uniform rotation calibration system was used similar to Ref. [20]. In this calibration process, a continuous servo motor (Geekstory Corp, Model DS04-NFC) with nine reflective beads was rotated at two different angular velocities: 0.52 rad/s and 5.02 rad/s, which gave two velocities ranges of beads as 0.025–0.225 m/s (0.52 rad/s) and 0.2–2.2 m/s (5.02 rad/s). The diagram of calibration setup is shown in Fig. 4. VPTV measured velocities were compared with calculated velocities to give the relative error of VPTV velocity measurement.

The average 3D velocity magnitudes and relative errors are shown in Fig. 5 (a) and (b). The mean relative errors $\bar{\delta}$ for rotation beads were 1.7% and 1.3% for the slow and fast velocity range, respectively. The mean error for slow and fast rotation trajectories were less than half of similar research [20]. Relative errors $\delta_{u,\,v,\,w}$ of x, y, and z velocity magnitudes components are shown in Fig. 5 (c), (d). All data points for $\delta_{u,\,v,\,w}$ were extracted from trajectories of beads at different time. The relative errors decrease exponentially as velocity magnitudes increase and remain steady when velocity magnitude is larger than 0.05 m/s for all three components.

It is observed that for velocity components larger than 0.2 m/s, some points are of larger relative error than velocity components smaller than 0.2 m/s. Possible reason is that the frame rates of cameras were set as 60 Hz/s for both fast and slow range. For fast moving particles, the spatial and temporal resolution of trajectories would be lower than slow moving particles. Therefore, the error introduced by fitting trajectories and calculating velocities would be larger than slow moving particles, and thus showed a more scattered pattern. However, since the average errors of both fast and slow velocity ranges are similar, this fitting error of specific velocity component would not influence the overall velocity magnitudes. To reduce the fitting error, a higher frame rate can be applied when tracking fast moving particles.

2.3. Measurement of anemometer

Streamwise velocity magnitudes at different positions around buildings were measured and compared between VPTV and hot-wire anemometer. The hot-wire anemometer with model TSI 8830 was used in this article and was calibrated with TSI 8390 wind tunnel. The accuracy of hot-wire anemometer is ±5.0% of reading or ±5 ft/min (±0.025 m/s) whichever is greater. The average relative error $\bar{\delta}_A$ is calculated using equation (1), where N is the total number of measurement points, w_A^i is the streamwise velocity magnitude of the i-th point measured by hot-wire anemometer, w_{VPTV}^i is the streamwise velocity magnitude of the i-th point measured by VPTV.

$$\bar{\delta}_A = \frac{1}{N}\sum_{i=1}^{N}\left|\frac{w_{VPTV}^i - w_A^i}{w_A^i}\right| \tag{1}$$

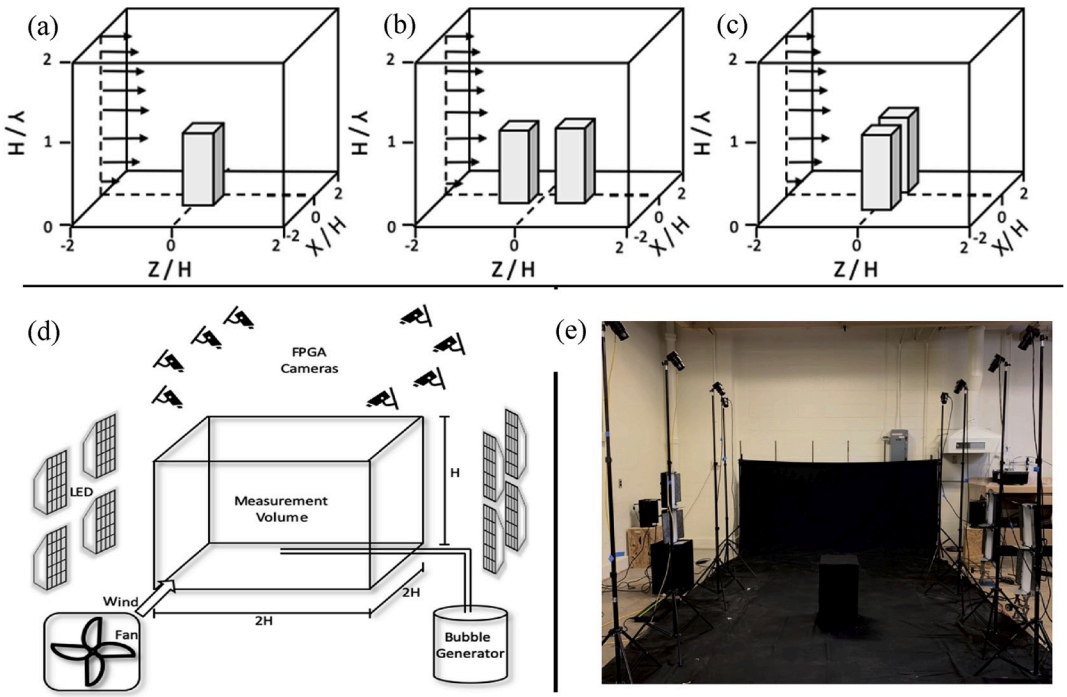

Fig. 7. (a) Single building; (b) Double building parallel to the wind; (c) Double building perpendicular to the wind; (d) Diagram of VPTV measurement system setup; (e) A photo of the experiment setup with a single building model.

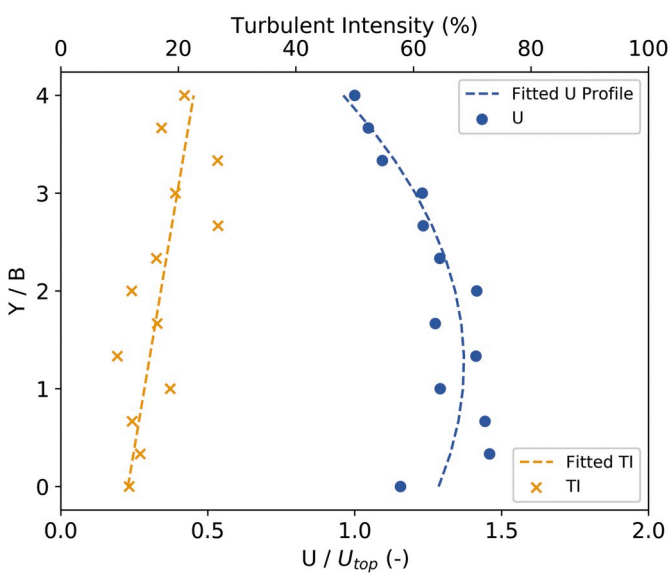

Fig. 8. Streamwise velocity profile and turbulent intensity of inlet wind.

2.4. Simulation of CFD

Streamlines and reattachment lengths measured by VPTV were compared with CFD simulations. The CFD simulations of single building setup was conducted by ANSYS FLUENT with standard $k-\varepsilon$ model. The computation domain is shown in Fig. 6 (a), where B is the building width. The meshes of cross-section Y = 0.5 H and X = 0 are shown in Fig. 6 (b) and (c). The grid was generated by Hex Dominant Method and there were 227077 tetrahedral cells in total. The grid independence analysis was done by increasing the mesh density up to 2 times and the results stayed steady. The hot-wire anemometer measurement data were used as inlet boundary conditions with 20% turbulent intensity. The outlet boundary condition was set as zero pressure. The wall boundary was set as non-slip boundary condition. The pseudo-transient pressure-velocity coupling scheme was applied for computation. For spatial discretization, least square cell based gradient, second order pressure, second order upwind momentum, first order upwind turbulent kinetic energy and first order upwind turbulent dissipation rate were used. The average relative error $\bar{\delta}_{CFD}$ was calculated using equation (2), where N is the total number of measurement points. In this case, 800 points uniformly distributed across cross-section X = 0 were selected. w^i_{CFD} is the velocity magnitude of the i-th point simulated by CFD, w^i_{VPTV} is the streamwise velocity magnitude of the i-th point measured by VPTV.

$$\bar{\delta}_{CFD} = \frac{1}{N}\sum_{i=1}^{N}\left|\frac{w^i_{VPTV} - w^i_{CFD}}{w^i_{CFD}}\right| \tag{2}$$

2.5. Experiments setup

In this experiment, three building setups were investigated as shown in Fig. 7 (a), (b), (c): single building, double building parallel to the wind and double building perpendicular to the wind. The building models were made of plywood and covered with black curtain to minimize light reflection. Each building model measured width 0.3 m, depth 0.3 m, and height 0.5 m.

The airflow was provided by a house fan through an expansion section. The inlet air flow rate was set approximately 0.5 m^3/s. The fan was placed in front of the first windward building cross-section with distance 2.1 m. The wind profile and turbulent intensity (TI) are shown in Fig. 8, where U is the streamwise velocity component magnitude and U_{top} is the U measured at top level. The Reynolds number of all setups were set around 10000 according to building dimension, which is often used as the Reynolds number threshold to achieve flow independent for bluff bodies with sharp edges [33]. The experiment setup diagram and real picture are shown in Fig. 7 (d), (e). The tracking particles were neutrally buoyant Helium-Filled soap Bubbles (HFSB) generated by a SAGE Action Model 5 bubble generator. A small vortex was used to ensure that only neutrally buoyant bubbles were released from the bubble generator. The average diameter of bubbles was 1.27 − 3.81 *mm*.

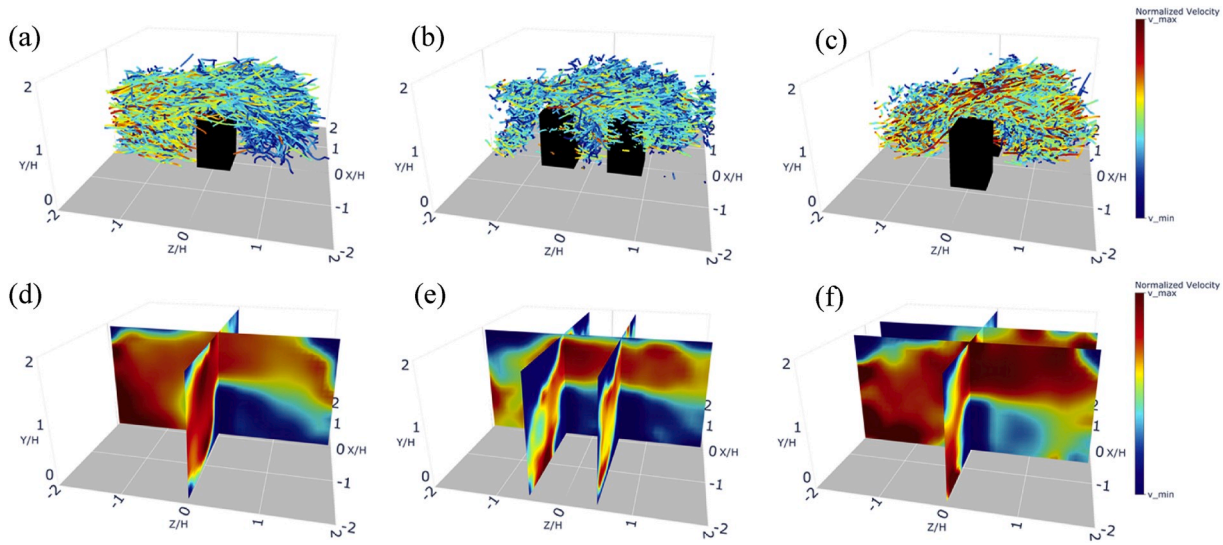

Fig. 9. (a) Trajectories near single building; (b) Trajectories near double building parallel to the wind; (c) Trajectories near double building perpendicular to the wind; (d) Cross-sections of velocity magnitudes across single building at $X = 0$ and $Z = 0$; (e) Cross-sections of velocity magnitudes across double building parallel with wind at $X = 0, Z = -1/2H$ and $Z = 1/2H$; (f) Cross-sections of velocity magnitudes across double building perpendicular with wind at $X = -1/2H, X = 1/2H$ and $Z = 0$.

Ten LED panels were used to illuminate VPTV measurement volume.

3. Results and discussion

3.1. Trajectories and local velocity

This system tracked abundant trajectories to give a statistical measurement of local velocities in measurement volume. The total trajectories number was 394671, 1616967 and 876910 for three setups, respectively. Partial trajectories near buildings during entire measurement period (30–60 min) are displayed in Fig. 9 (a) and (b), (c), and the statistical velocity distribution are shown in Fig. 9 (d) and (e), (f). The positive Z axis is the streamwise direction. The test volume includes $X/H \in (-2, 2)$, $Y/H \in (0, 1)$ and $Z/H \in (-2, 2)$, where H is the building height. The origin location $(X, Y, Z) = (0, 0, 0)$ is at the center of plane $Y = 0$.

For the single building case, bypassing building flow can be observed by the trajectories near the building. For two buildings parallel to the wind direction, low speed trajectories were trapped between buildings. For the last perpendicular setup, trajectories within buildings gap had larger speed because of amplification effect. Thus, all major characteristics of flow field can be captured and represented by trajectories measured by the VPTV system.

This VPTV system can cover nearly the entire measurement volume in terms of the local velocity interpolation. Cross-sections for different setups are shown as follows: For the single building setup, the cross-sections were at $X = 0$ and $Z = 0$. For double building parallel to the wind, cross-sections were at $X = 0$, $Z = -1/2H$ and $Z = 1/2H$. For double building perpendicular to the wind, cross-sections were at $X = -1/2H$, $X = 1/2H$ and $Z = 0$. Interpolated local velocity can also be used to identify the main characteristics of building wind environments. For example, high speed flow before encountering buildings, separated flow by buildings and vortexes between and behind buildings can be clearly visualized.

3.2. Streamlines of 2D cross-sections

To better represent the flow patterns, streamlines of 2-D cross-sections of interest for three setups are shown in Fig. 10. Streamlines of single building setup are shown in Fig. 10 (a)–(d). The observed flow patterns of single building were similar to the typical flow patterns observed around bluff building stated by Ref. [34]: impingement area, flow separation, shear layer and recirculation. Impingement flow was observed in front of building models. Meanwhile, flow separation was observed above building. Flow bypassed building upwards and no downward flow or vortex were observed. A shear layer was visible right above the building with a positive velocity gradient. A primary vortex with radius approximately half building height was observed behind the building. A recirculation zone at the floor behind the building model was also observed.

For the two buildings parallel to the wind setup in Fig. 10 (e)–(h), primary interest area is the gap between two buildings, which represents street canyon perpendicular to the wind. Two vortexes can be observed in the building gap. The first one is the primary vortex rotating clockwise from $y \varepsilon (H/4, H)$. The second one can be identified by streamlines at the lower part of building channel rotating counterclockwise. The second vortex is generated when the aspect ratio of building model (Height/Width) is larger than 1.6 [35].

For the two buildings perpendicular to the wind direction in Fig. 10 (i)–(l), the gap between two buildings is supposed to amplify the airflow speed. There is no vortex observed close to adjacent sides of the buildings. However, a vortex was formed at X = 0.6 H and extended to larger scale at X = 0.9 H. The overall flow pattern is similar with what Shen et al. [36] has found by CFD simulation of street canyon flow in similar setup.

3.3. Comparison of VPTV measurement with anemometry

The comparison of time averaged local streamwise velocity magnitudes between VPTV and hot-wire anemometer are shown in Fig. 11. All measurement points were on center plane X = 0. The overall relative error between hot-wire anemometer and VPTV results is 26.18%. In general, anemometer tends to over measure the streamwise velocity magnitude. Possible reason is that hot-wire anemometer is intrusive for flow field. Local flow is forced to flow streamwise through measurement chamber. When other direction velocity components are supposed to exist, streamwise velocity magnitudes would be over measured by anemometer. This trend is clearly observed in Fig. 11 (c), where all data points have significant Y velocity component according to Fig. 10 (i).

Error bars in Fig. 11 represents the standard deviation of local velocities, higher value means it is more turbulent at specific points. Generally, VPTV has larger standard deviation than anemometer.

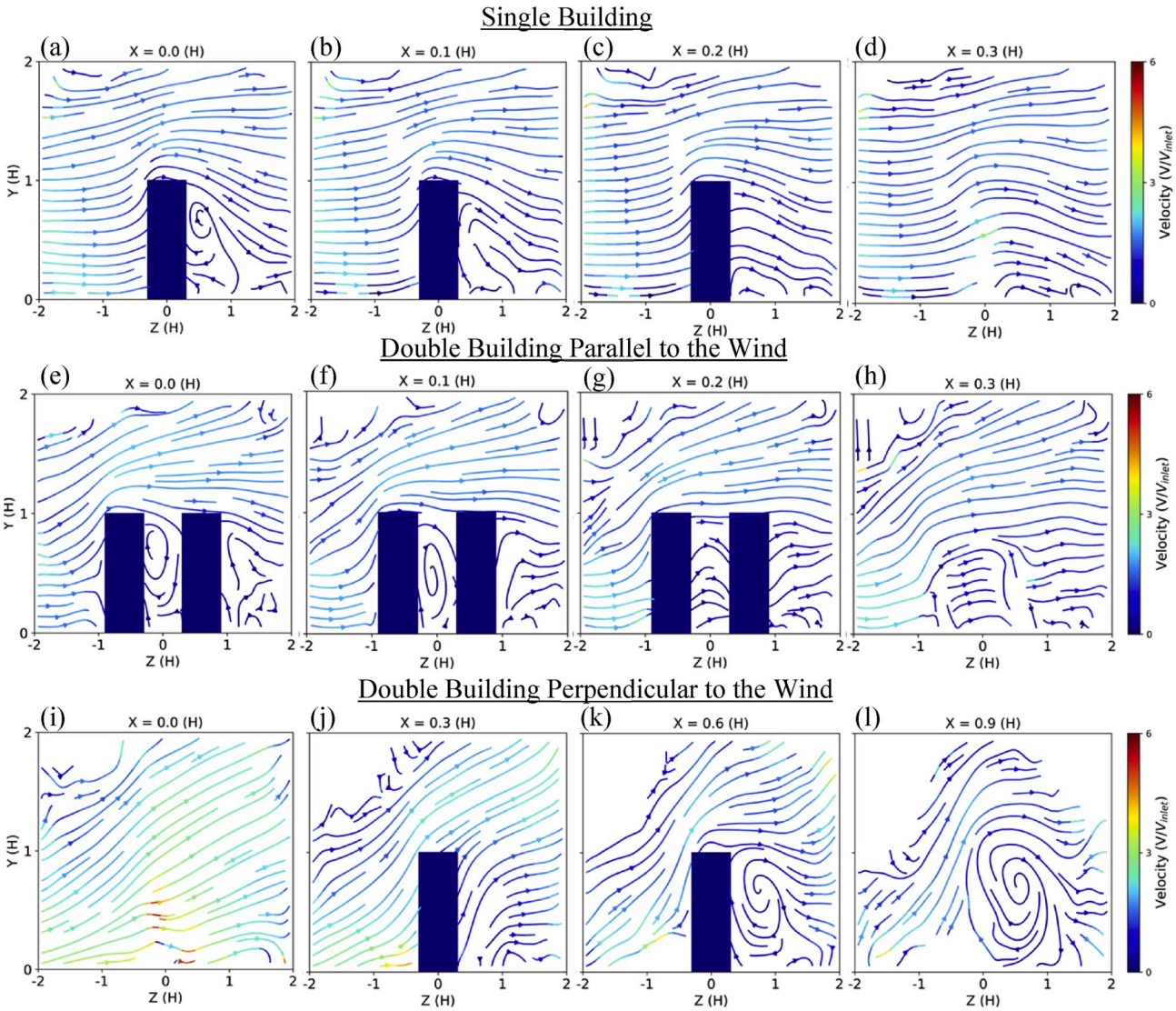

Fig. 10. Streamlines of 2-D cross-sections of different setups. a. YZ cross-sections of streamlines from X = 0–0.3 H with an interval 0.1 H, where H is the building height; b. cross-sections of streamlines from X = 0–0.3 H with an interval 0.1H; c. cross-section of streamlines from X = 0–0.9 H with an interval 0.3 H.

Possible reason is that more detailed flow can be captured because of higher temporal resolution of VPTV.

3.4. Comparison with CFD simulation

3.4.1. Comparison of streamlines

In this comparison, only the single building setup was simulated and compared, as it is more widely studied than the other two setups. Streamlines at plane X = 0 measured by VPTV and simulated by CFD are shown in Fig. 12. CFD simulation of this cross-section showed similar results with cross-section measured by VPTV. The main vortex behind building is successfully represented by both VPTV and CFD. The positions and scales of both vortexes showed great correspondence. However, VPTV detected a second vortex near floor, which is not observed by CFD. The overall relative error between CFD simulation and VPTV measurement on this plane is 16.33%. Shao et al. [37] simulated similar geometry building and generated streamlines with different turbulence models. Their standard $k-\varepsilon$ model simulation also has similar streamlines with our CFD simulation results.

3.4.2. Comparison of reattachment lengths

To conduct a more numerical comparison, reattachment lengths above building X_R and behind building X_F are chosen, as they are important properties of BWE study. In this article, reattachment point is defined as the position with 50% forward streamwise velocity. The diagram of reattachment lengths is shown in Fig. 13 (a). The reattachment length X_R is statistically determined as sufficient trajectories are tracked above building. For reattachment length X_F, it is calculated based on method [38] because of insufficient trajectories near floor, the data points used to predict X_F are shown in Fig. 13 (b).

The reattachment length X_R of single building setup was 0.42 times of building width, which is similar with an experiment study [39]. The reattachment length X_F was 2.27 times of building width. This number is between the results of CFD simulations [40] and experiment [39]. For reattachment length X_F, VPTV method takes advantage of larger resolution compared to previous experimental research and gives similar result to CFD simulation. The reattachment length X_F of [39] is 1.42 times of building width and X_F of experiment work [41] is around 1.25. All reattachment lengths of different research but with similar setup are shown in Table 1.

4. Discussions

There were several aspects affecting the accuracy of measurement.

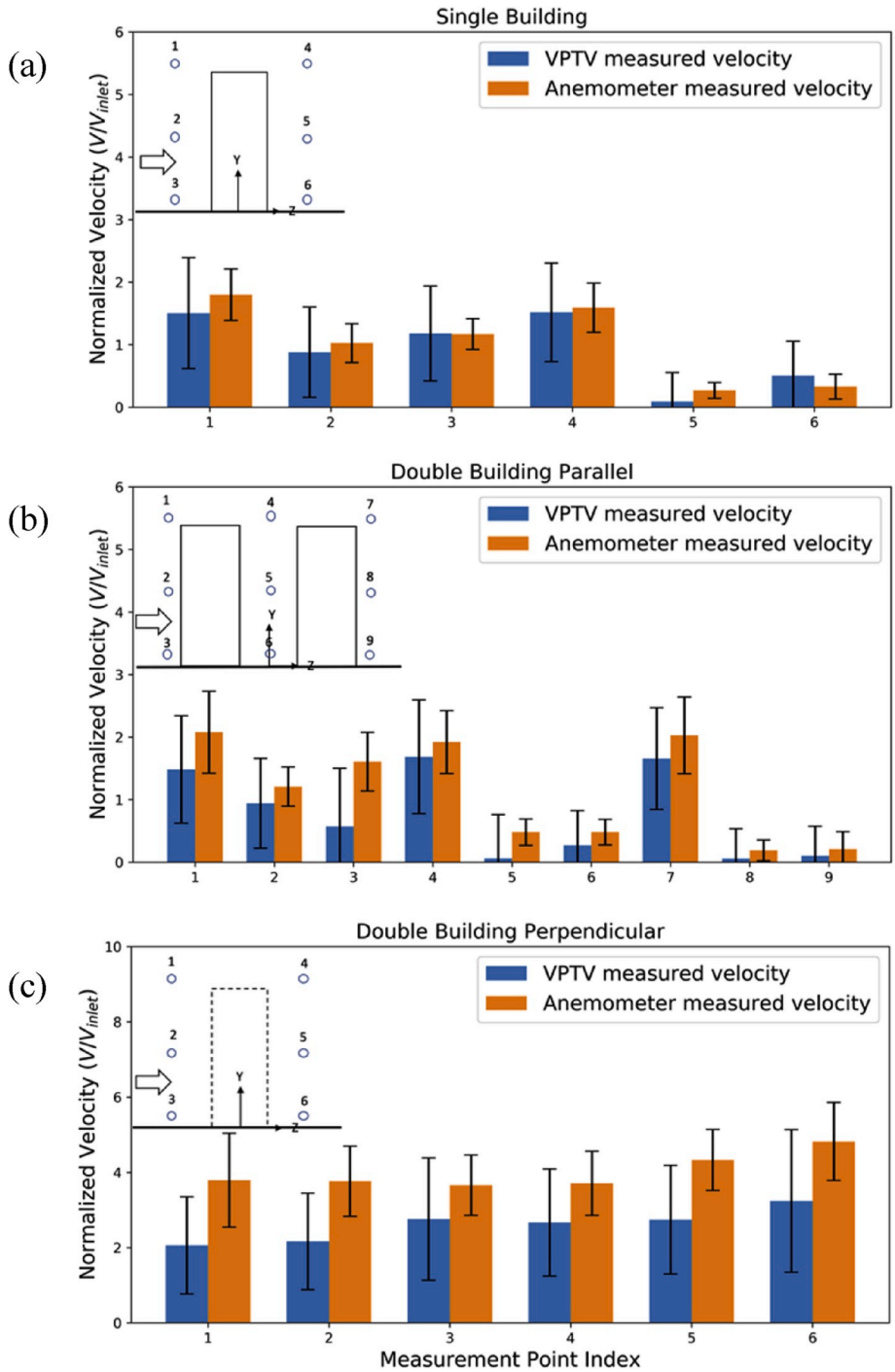

Fig. 11. Comparison of streamwise velocities magnitudes at cross-sections X = 0 from three setups. The inner diagram represents where the points are located. (a) Single building measurements; (b) Double building parallel to the wind measurements; (c) Double building perpendicular to the wind measurement.

Reflection of buildings and floor would generate false detected particles, however only small part of measurement volume would be influenced, and post processing of data can be applied to remove false detected particles.

Although sparse particle distribution can be caused by open measurement volume. Low data transfer rate of FPGA camera allows long measurement time window (30–60 min), which will compensate the low particle density and track enough particles for analysis.

Particles could be unevenly distributed; the possible reason is that the experiment setup was not perfectly symmetrical. To solve this problem, the inlet of tracing particles can be modified to balance the particle density of different area in measurement volume.

5. Conclusions

In this paper, 3D flow patterns of high-rise building models were measured using a real-time volumetric particle tracking velocimetry. Specifically, this study has demonstrated that:

1. The Lagrangian velocity measured by VPTV system was calibrated against known trajectory velocities with relative error smaller than 2%;

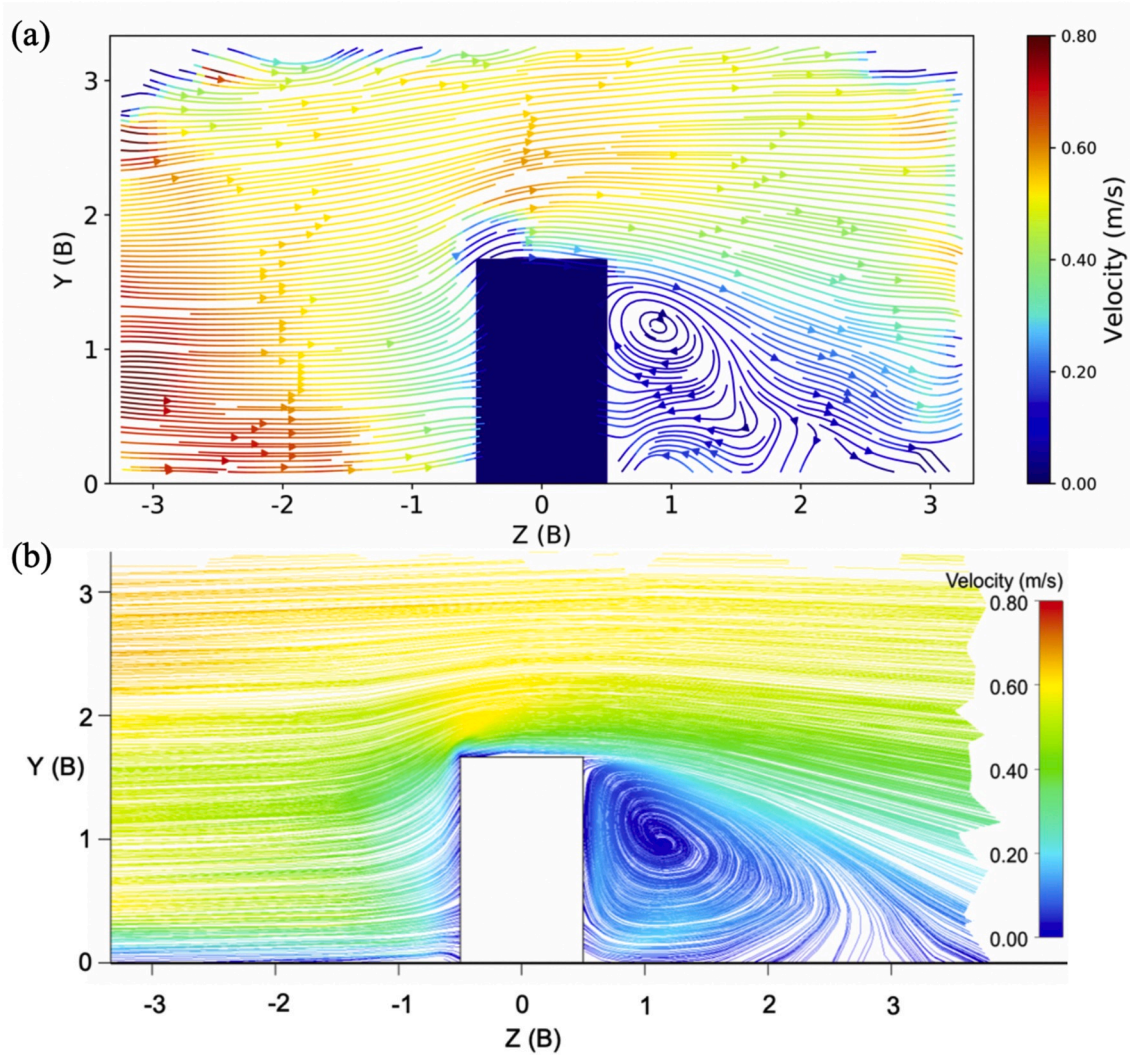

Fig. 12. Streamlines of high-rise building, where B is the building width. (a) Streamlines measured by VPTV results of single building setup at plane X = 0; (b) Streamlines simulated by CFD at plane X = 0 with same geometry.

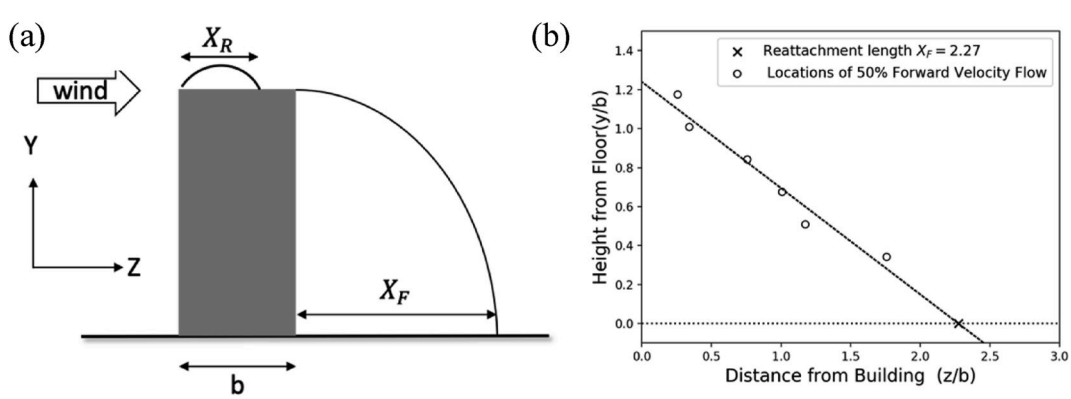

Fig. 13. (a) Diagram of building with width b, reattachment lengths X_R and X_F; (b) Locations with 50% streamwise velocity and predicted X_F.

2. Eulerian velocity distribution interpolated by VPTV system was similar with hot-wire anemometer with explainable deviation. Moreover, VPTV can provide much more information than hot-wire anemometer in terms of spatial resolution and complete distribution of velocity spectrum;
3. Flow patterns measured by VPTV are accurate, informative and can be used to validate CFD simulation. VPTV measurement reveals specific characteristics of wind environment around buildings by tracking trajectories, local velocities, critical vortexes, streamlines and reattachment lengths.

In summary, VPTV is a flexible technique that measures flow patterns by tracking Lagrangian particle trajectories and yields accurate and informative results. The measured data can be used to aid building

Table 1
Comparison of reattachment lengths.

	Turbulence Model		X_R/b	X_F/b
CFD [39]	SRANS	Standard k-ε	–	2.5
		RNG k-ε	0.6	3.05
		Realizable k–ε	–	3.05
		Standard k–ω	–	2.78
		k–ω SST	>1	4.06
	URANS	k–ω SST	>1	2.91
		RNG k–ε with modified ε-equation	0.84	2.90
CFD (ours)		Standard k-ε	–	2.40
Experiment [39]	–		0.52	1.42
Experiment [41]	–		–	1.25
Experiment (ours)	–		0.42	2.27

environment design and as boundary conditions to conduct accurate CFD simulation.

Declaration of competing interest

All the authors declare that they have no known competing financial interests or personal relationships that could have appeared to influence the work reported in this paper.

Acknowledgements

The authors acknowledge the support from National Natural Science Foundation of China (Grant No. 51578065) and National Natural Science Foundation of Beijing (Grant No. 8182019) to Dr. Xiaojun Ma and Dr. Haoyu Wang respectively, to allow their collaboration and visiting abroad.

References

[1] L.S. Beedle, M.M. Ali, P.J. Armstrong, The Skyscraper and the City: Design, Technology, and Innovation, Lewiston, Mellen, 2007.
[2] C. Yuan, E. Ng, L.K. Norford, Improving air quality in high-density cities by understanding the relationship between air pollutant dispersion and urban morphologies, Build. Environ. 71 (2014) 245–258, https://doi.org/10.1016/j.buildenv.2013.10.008.
[3] Y. Tominaga, T. Stathopoulos, CFD Modeling of Pollution Dispersion in Building Array: evaluation of turbulent scalar flux modeling in RANS model using LES results, J. Wind Eng. Ind. Aerod. 104–106 (2012) 484–491, https://doi.org/10.1016/j.jweia.2012.02.004.
[4] J. Hang, Y. Li, M. Sandberg, R. Buccolieri, S.D. Sabatino, The influence of building height variability on pollutant dispersion and pedestrian ventilation in idealized high-rise urban areas, Build. Environ. 56 (2012) 346–360, https://doi.org/10.1016/j.buildenv.2012.03.023.
[5] LEED V4 for Building Design and Construction, 2020 accessed, https://www.usgbc.org/guide/bdc. (Accessed 16 April 2020).
[6] BRE, BREEAM communities. Technical Guidance Manual. Stage 2 Version 1, Building Research Establishment, Watford, UK, 2011.
[7] T. Kubota, M. Miura, Y. Tominaga, A. Mochida, Wind tunnel tests on the relationship between building density and pedestrian-level wind velocity: development of guidelines for realizing acceptable wind environment in residential neighborhoods, Build. Environ. 43 (10) (2008) 1699–1708, https://doi.org/10.1016/j.buildenv.2007.10.015.
[8] C. Tsang, K. Kwok, P. Hitchcock, Wind tunnel study of pedestrian level wind environment around tall buildings: effects of building dimensions, separation and podium, Build. Environ. 49 (2012) 167–181, https://doi.org/10.1016/j.buildenv.2011.08.014.
[9] S.G. Perry, D.K. Heist, R.S. Thompson, W.H. Synder, R.E. Lawson Jr., Wind Tunnel Simulation of Flow and Pollutant Dispersal Around the World Trade Center Site, 2004, pp. 31–34.
[10] M. Lateb, R. Meroney, M. Yataghene, H. Fellouah, F. Saleh, M. Boufadel, On the use of numerical modelling for near-field pollutant dispersion in urban environments – A review, Environ. Pollut. 208 (2016) 271–283, https://doi.org/10.1016/j.envpol.2015.07.039.
[11] L. Li, X. Yang, Y. Qian, CFD simulation analysis of the influence of floor area ratio on the wind environment in residential districts, J. Eng. Sci. Technol. Rev. 11 (5) (2018) 185–192, https://doi.org/10.25103/jestr.115.24.
[12] Y.J. Wu, Z.H. Chen, T. Sun, X. Deng, Numerical simulation of wind interference among tall buildings and analysis of its wind environment, in: International Conference on Mechanic Automation and Control Engineering, 2010, https://doi.org/10.1109/mace.2010.5535776.
[13] X. Chen, G. Xu, Numerical simulation and evaluation of wind environment about square earth buildings, in: International Conference on Consumer Electronics, Communications and Networks (CECNet), 2011, https://doi.org/10.1109/cecnet.2011.5769283.
[14] B. Hong, H. Qin, B. Lin, Prediction of wind environment and indoor/outdoor relationships for PM2.5 in different building–tree grouping patterns, Atmosphere 9 (2) (2018) 39, https://doi.org/10.3390/atmos9020039.
[15] R.J. Adrian, Particle-imaging techniques for experimental fluid mechanics, Annu. Rev. Fluid Mech. 23 (1) (1991) 261–304, https://doi.org/10.1146/annurev.fl.23.010191.001401.
[16] R.D. Keane, R.J. Adrian, Theory of cross-correlation analysis of PIV images, in: Fluid Mechanics and its Applications Flow Visualization and Image Analysis, 1993, pp. 1–25, https://doi.org/10.1007/978-94-011-2690-8_1.
[17] A. Liberzon, R. Gurka, G. Hetsroni, XPIV-Multi-plane stereoscopic particle image velocimetry, Exp. Fluid 36 (2) (2004) 355–362, https://doi.org/10.1007/s00348-003-0731-9.
[18] G.E. Elsinga, B. Wieneke, F. Scarano, A. Schröder, Tomographic 3D-PIV and applications, Top. Appl. Phys. Image Velocimetry 112 (2007) 103–125, https://doi.org/10.1007/978-3-540-73528-1_6.
[19] Y. Sun, Volumetric Particle Streak-Tracking Velocimetry and its Application in Indoor Airflow Measurements. (Doctoral Dissertation), University of Illinois at Urbana-Champaign, 2007.
[20] H. Wang, X. Li, X. Shao, B. Wang, Y. Lin, A colour-sequence enhanced particle streak velocimetry method for air flow measurement in a ventilated space, Build. Environ. 112 (2017) 77–87, https://doi.org/10.1016/j.buildenv.2016.11.015.
[21] D. Schanz, S. Gesemann, A. Schröder, Shake-The-Box: Lagrangian particle tracking at high particle image densities, Exp. Fluid 57 (5) (2016), https://doi.org/10.1007/s00348-016-2157-1.
[22] M. Kreizer, A. Liberzon, Three-dimensional particle tracking method using FPGA-based real-time image processing and four-view image splitter, Exp. Fluid 50 (3) (2010) 613–620, https://doi.org/10.1007/s00348-010-0964-3.
[23] D. Barker, J. Lifflander, A. Arya, Y. Zhang, A parallel algorithm for 3D particle tracking and Lagrangian trajectory reconstruction, Meas. Sci. Technol. 23 (2) (2011), 025301, https://doi.org/10.1088/0957-0233/23/2/025301.
[24] B. Douglas, Z. Yuanhui, R.S. Gates, A.M. Jacobi, B.G. Thomas, Y. Sun, Development of a Scalable Real-Time Lagrangian Particle Tracking System for Volumetric Flow Field Characterization. (Doctoral Dissertation), University of Illinois at Urbana-Champaign, Urbana, Illinois, 2012.
[25] J.C. Crocker, D.G. Grier, Methods of digital video microscopy for colloidal studies, J. Colloid Interface Sci. 179 (1) (1996) 298–310, https://doi.org/10.1006/jcis.1996.0217.
[26] G.A. Rosi, M. Sherry, M. Kinzel, D.E. Rival, Characterizing the lower log region of the atmospheric surface layer via large-scale particle tracking velocimetry, Exp. Fluid 55 (5) (2014), https://doi.org/10.1007/s00348-014-1736-2.
[27] J.-T. Kim, Z. Zhang, A. Liberzon, Y. Zhang, L. Chamorro, On the Lagrangian features of circular and semicircular jets via 3D Particle Tracking Velocimetry, Exp. Therm. Fluid Sci. 77 (2016) 306–316, https://doi.org/10.1016/j.expthermflusci.2016.05.003.
[28] Y. Hui, Y. Tamura, A. Yoshida, H. Kikuchi, Pressure and flow field investigation of interference effects on external pressures between high-rise buildings, J. Wind Eng. Ind. Aerod. 115 (2013) 150–161, https://doi.org/10.1016/j.jweia.2013.01.012.
[29] H.G. Maas, A. Gruen, D. Papantoniou, Particle tracking velocimetry in three-dimensional flows: Part 1. Photogrammetric determination of particle coordinates, Exp. Fluid 15 (2) (1993) 133–146.
[30] Z. Zhang, A flexible new technique for camera calibration, IEEE Trans. Pattern Anal. Mach. Intell. 22 (11) (2000) 1330–1334, https://doi.org/10.1109/34.888718.
[31] P.H. Biwole, W. Yan, Y. Zhang, J. Roux, A complete 3D particle tracking algorithm and its applications to the indoor airflow study, Meas. Sci. Technol. 20 (11) (2009) 115403, https://doi.org/10.1088/0957-0233/20/11/115403.
[32] D. Li, Y. Zhang, Y. Sun, W. Yan, A multi-frame particle tracking algorithm robust against input noise, Meas. Sci. Technol. 19 (10) (2008) 105401, https://doi.org/10.1088/0957-0233/19/10/105401.
[33] N. Isyumov, J.E. Cermak, Wind Tunnel Studies of Buildings and Structures, ASCE, Reston, 1999, pp. 14–15.
[34] B. Blocken, T. Stathopoulos, J.V. Beeck, Pedestrian-level wind conditions around buildings: review of wind-tunnel and CFD techniques and their accuracy for wind comfort assessment, Build. Environ. 100 (2016) 50–81, https://doi.org/10.1016/j.buildenv.2016.02.004.
[35] S.-J. Park, J.-J. Kim, M.J. Kim, R.J. Park, H.-B. Cheong, Characteristics of flow and reactive pollutant dispersion in urban street canyons, Atmos. Environ. 108 (2015) 20–31, https://doi.org/10.1016/j.atmosenv.2015.02.065.
[36] Z. Shen, B. Wang, G. Cui, Z. Zhang, Flow pattern and pollutant dispersion over three-dimensional building arrays, Atmos. Environ. 116 (2015) 202–215, https://doi.org/10.1016/j.atmosenv.2015.06.022.
[37] J. Shao, J. Liu, J. Zhao, Evaluation of various non-linear k–ϵ models for predicting wind flow around an isolated high-rise building within the surface boundary layer, Build. Environ. 57 (2012) 145–155, https://doi.org/10.1016/j.buildenv.2012.04.018.
[38] N. Kasagi, A. Matsunaga, S. Kawara, Turbulence measurement in a separated and reattaching flow over a backward-facing step with the aid of three-dimensional particle tracking velocimetry, Comput. Wind Eng. 1 (1993) 821–829, https://doi.org/10.1016/b978-0-444-81688-7.50093-0.

[39] Y. Meng, K. Hibi, Turbulent measurments of the flow field around a high-rise building, Wind Eng. JAWE 1998 (76) (1998) 55–64, https://doi.org/10.5359/jawe.1998.76_55.

[40] Y. Tominaga, Flow around a high-rise building using steady and unsteady RANS CFD: effect of large-scale fluctuations on the velocity statistics, J. Wind Eng. Ind. Aerod. 142 (2015) 93–103, https://doi.org/10.1016/j.jweia.2015.03.013.

[41] R. Martinuzzi, C. Tropea, The flow around surface-mounted, prismatic obstacles placed in a fully developed channel flow (data bank contribution), J. Fluid Eng. 115 (1) (1993) 85–92, https://doi.org/10.1115/1.2910118.